A Robust Method for Ultrasound Beamforming in the Presence of Off-Axis Clutter and Sound Speed Variation

Kazuyuki Dei*, Brett Byram

Department of Biomedical Engineering, Vanderbilt University, Nashville, TN, USA

ABSTRACT

Previously, we introduced a model-based beamforming algorithm to suppress ultrasound imaging artifacts caused by clutter sources, such as reverberation and off-axis scattering. We refer to this method as aperture domain model image reconstruction (ADMIRE). In this study, we evaluated the algorithm's limitations and ability to suppress off-axis energy using Field II-based simulations, experimental phantoms and *in vivo* data acquired by a Verasonics ultrasound system with a curvilinear transducer (C5-2). We compared image quality derived from a standard delay-and-sum (DAS) beamformer, DAS with coherence factor (CF) weighting, ADMIRE and ADMIRE plus CF weighting. Simulations, phantoms and *in vivo* scan results demonstrate that ADMIRE substantially suppresses off-axis energy, while preserving the spatial resolution of standard DAS beamforming. We also observed that ADMIRE with CF weighting further improves some aspects of image quality. We identified limitations of ADMIRE when suppressing off-axis clutter in the presence of strong scattering, and we suggest a solution. Finally, because ADMIRE is a model-based beamformer, we used simulated phantoms to test the performance of ADMIRE under model-mismatch caused by gross sound speed deviation. The impact of sound speed errors largely mimics DAS beamforming, but ADMIRE never does worse than DAS itself in resolution or contrast. As expected the CF weighting used as a post processing technique provides a boost in contrast but decreases CNR and speckle SNR. The results indicate that ADMIRE is robust in terms of model-mismatch caused by sound speed variation, especially when the actual sound speed is slower than the assumed sound speed. As an example, the image contrast obtained using DAS, DAS + CF, ADMIRE and ADMIRE + CF in the presence of -5% gross sound speed error are 24.9 $\pm$ 0.71 dB, 39.1 $\pm$ 1.2 dB, 43.2 $\pm$ 2.3 dB and 52.5 $\pm$ 2.9 dB, respectively.

1. Introduction

Ultrasound is one of the most widely used imaging modalities in medicine and has been used extensively for diagnosis and therapy due to its real-time, inexpensive and non-invasive features [1]. Ultrasound suffers from many artifacts, which impair image quality and limit its effectiveness [2–8]. These artifacts degrade the resolution and contrast of an ultrasound image, and subsequently reduce the usefulness of ultrasound in diagnosis and therapeutic guidance [9].

It is well-established that lower point spread function side-lobes are correlated with higher contrast and that narrower main-lobe width provides better spatial resolution. Conventional beamforming, often referred to as delay-and-sum (DAS), in conjunction with a deterministic apodization scheme, such as Hamming, Hann or Gaussian window function, can improve contrast by suppressing side-lobes but at the cost of broadening the main-lobe, which degrades spatial resolution. Alternatively, DAS with rectangular apodization yields better resolution but lower contrast because of higher side-lobes.

In order to address the trade-off encountered with traditional apodization methods, many adaptive beamforming algorithms have been developed and evaluated, including coherence-based adaptive weighting [10–13], minimum variance beamforming [14–18], dual apodization using cross-correlation [19–21], non-linear apodization techniques such as dual-/tri-apodization with chosen window functions [22], apodization profiling methods using constrained least squares [23,24] and the second-order-cone optimization [25]. A side-lobe filtering method has also been reported to have had substantial effects on ultrasound image quality [26].

Our group introduced a model-based beamforming algorithm [8,27–30]. The algorithm uses a model of received wavefronts on aperture domain signals reflected from scatterers located in the imaging field of interest. The model enables the algorithm to identify scatterer locations and suppress clutter, particularly, off-axis scattering and reverberation artifacts. We refer to the algorithm as aperture domain

model image reconstruction (ADMIRE). ADMIRE decomposes the aperture domain signals into clutter and signal of interest components. The clutter component is removed, leaving decluttered channel data behind. While ADMIRE has been shown to suppress reverberation artifacts [29,31], the primary objective here is to demonstrate whether ADMIRE suppresses off-axis clutter without sacrificing the resolution obtained from an unapodized beam. In this study, the model space is specifically restricted to only depths around the region of interest so that the algorithm primarily accounts for off-axis clutter. Because AD-MIRE preserves decluttered channel data, we can also combine ADMIRE with other methods to investigate whether additional post processing techniques further improve image quality. There are many potential algorithms that may enable post-ADMIRE decluttered signals to achieve further off-axis suppression and improve image quality. In this study, we used a coherence factor (CF) weighting technique, which was originally introduced by Mallart and Fink [10], also formalized as a metric by Hollman et al. [11]. The coherence factor is useful to weight delayed channel data (i.e., aperture domain signals) without introducing a high computational complexity.

To further evaluate the ADMIRE algorithm, we investigated whether ADMIRE, a model-based beamformer, is robust to model-mismatch caused by deviations in gross sound speed. Clinical ultrasound image formation typically assumes a constant speed of sound of 1540 m/s. However, *in vivo* sound speed is not constant and tissues have velocities ranging from 1400 m/s to 1650 m/s that cause variation in the overall effective sound speed [4]. These gross sound speed deviations degrade image quality by reducing contrast and spatial resolution [5].

In this paper, we provide an overview of the ADMIRE algorithm and evaluate the algorithm's robustness in the presence of off-axis clutter using simulations performed with Field II and experimental measurements from phantoms and *in vivo data* acquired using an ultrasound imaging system. In simulations, we tested the performance of ADMIRE, ADMIRE plus CF weighting, compared to DAS with and without CF, using point spread functions and resolution target phantoms. We also captured experimental data from a wire phantom, a tissue-mimicking phantom and a human subject liver. In evaluating ADMIRE, we also identified some limitations and demonstrate solutions. Finally, we show the impact of ADMIRE in the presence of sound speed variation from two target simulation cases—(1) resolution target and (2) contrast target. In resolution target simulations, we measured the lateral full-width at half-maximum (FWHM) of the main-lobe with respect to a ratio of gross sound speed errors, while image quality metrics (i.e., contrast and contrast-to-noise ratio) and speckle statistics (i.e., speckle signal-to-noise ratio) were used in the case of contrast target simulations.

2. Methods

2.1. Model-based beamforming

The model used for ADMIRE accounts for spherical wavefronts, short-time Fourier Transform (STFT), pulse-bandwidth correction and angular sensitivity, leading to a non-stationary, sinusoidal model [29]. The basic model can be expressed as

$$p_s(x;t,\omega) = \sum_{n=0}^{N-1} A_n(x) e^{j\omega\tau(x;x_n,z_n,\tau_n)}, \tag{1}$$

where p_s is the scattered pressure, x is the aperture position, t and ω are the time and frequency of the localized signal, $\tau(x;x_n,z_n,\tau_n)$ is the wavefront delay for a received echo signal scattering from point (x_n,z_n) at time τ_n and N is the number of scatterers arriving at time t. $A_n(x)$ is derived from two terms: (1) element sensitivity ($A_{ES}(x)$), indicated by Selfridge et al.'s findings [32] and (2) the axial STFT window effects ($A_{STFT}(x)$), given by,

$$A_n(x) = A_{ES}(x)A_{STFT}(x). \tag{2}$$

The second-term of (2) depends on the signal's pulse shape and $\tau(x;x_n,z_n,\tau_n)$, as follows [29].

$$A_{STFT}^2(x) = \int_{t_c-\frac{\Delta t}{2}}^{t_c+\frac{\Delta t}{2}} w_{STFT}^2(t-t_c)w_{env}^2(t-\tau(x;x_n,z_n,\tau_n))\,dt, \tag{2a}$$

where Δt is the STFT window width, t_c is the middle of the STFT window, denoted as w_{STFT}, and w_{env} is the axial pulse envelope function.

The STFT is applied to the delayed channel signals at a small range of depths to convert the signal into the frequency domain. A single frequency of the post-STFT signal at a given depth, denoted as y, is defined in the following matrix form.

$$y = [\Re\{S_i(mT,\omega_p)\} \;\; \Im\{S_i(mT,\omega_p)\}]^\top, \tag{3}$$

where $\Re$ and $\Im$ denote the real and imaginary components, respectively, mT is the discrete time index, T is the sampling period of the channel data, ω_p is a discrete frequency, $S_i(mT,\omega_p)$ is the post-STFT signal for a single channel of the aperture, i indexes channel and $\top$ denotes the matrix transpose. Next, we construct ADMIRE model predictors with the specific model space sampling using the basic ADMIRE model in (1), given by

$$X = \begin{bmatrix} \Re\{p_{s_n}(x;t,\omega)\}^\top & -\Im\{p_{s_n}(x;t,\omega)\}^\top \\ \Im\{p_{s_n}(x;t,\omega)\}^\top & \Re\{p_{s_n}(x;t,\omega)\}^\top \end{bmatrix}. \tag{4}$$

Fig. 1 shows an ADMIRE model matrix and the corresponding model space. As described in the figure, the ADMIRE model space has two subspaces: (1) region of interest (ROI) subspace and (2) clutter subspace.

A single frequency of the aperture domain signal in (3) can be written in a linear model using the ADMIRE model matrix in (4) by,

$$y = X\beta, \tag{5}$$

where β is the model coefficient vector for the predictors in X. However, because solving for β in (5) is ill-posed, β in (5) can be estimated using elastic-net regularization [33]. This model-fit (i.e., model decomposition) may be expressed as

$$\hat{\beta} = \min_\beta \left(\|y - X\beta\|^2 + \lambda(\alpha\|\beta\|_1 + (1-\alpha)\|\beta\|_2^2/2) \right), \tag{6}$$

where $\|\beta\|_1$ and $\|\beta\|_2$ denote the L1 norm and L2 norm, respectively, and α and λ terms determine the degree and type of regularization. The parameter of α adjusts the relative weight of L1 and L2 norms between 0 and 1. The degrees of freedom (df), which are a function of λ, reported by Tibshirani et al. [34], play a crucial role in the performance
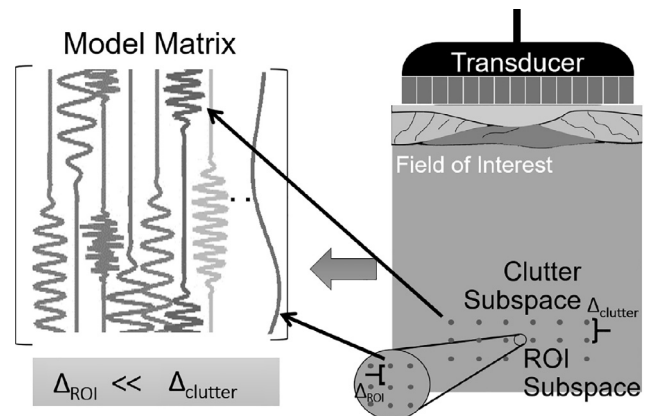
Fig. 1. ADMIRE matrix of model predictors with the specific model space sampling. The ADMIRE model space has two subspaces: (1) region of interest (ROI) subspace and (2) clutter subspace. The ADMIRE model space is finely sampled in the ROI subspace and coarsely sampled in the clutter subspace. In this study, the model space is specifically restricted to only depths around the region of interest so that the algorithm primarily accounts for off-axis clutter.

of ADMIRE [29,30,35].

We then select predictors from within the acceptance zone, in order to reconstruct decluttered channel signals, given by

$$y_{SOI} = X_{SOI}\hat{\beta}_{SOI},\tag{7}$$

where y_{SOI} is a decluttered signal, X_{SOI} is the model with predictors that are spatially within the ROI and $\hat{\beta}_{SOI}$ is the corresponding model coefficients. The acceptance zone is specified as an ellipse based on the expected lateral and axial resolutions of res_{lat} and res_{axl}, respectively, given by

$$\left(\frac{x_n - x_r}{c_{lat}\,res_{lat}}\right)^2 + \left(\frac{z_n - z_r}{c_{axl}\,res_{axl}}\right)^2 \leqslant 1,\tag{8}$$

where x_r and z_r denote the center of the acceptance zone, and c_{lat} and c_{axl} are scalable factors for the acceptance region laterally and axially, respectively. In this study, res_{lat} is computed by $res_{lat} \approx \lambda_w z \mathscr{F}\{|p_s(x;x_r,z_r,0)|\}_{BW}$ while the axial sampling is approximated by $res_{axl} \approx 2res_{lat}$, where λ_w is the wavelength, z is the axial depth, $F\{|\cdot|\}_{BW}$ denotes the lateral bandwidth of the model predictor [29,36].

The decluttered signal in the frequency domain is transformed back to the time domain using the inverse short-time Fourier Transform (ISTFT) [37]. In this study, the ADMIRE model space is restricted to the depth around the acceptance zone so that the algorithm primarily focuses on off-axis clutter rejection. Table 1 shows the parameters used unless otherwise specified.

Note that the selection of these regularized parameters was determined by simulations findings from a previous study [29].

2.2. Coherence factor

As an additional comparison, we consider the coherence factor on its own and as an additional post-processing after ADMIRE. To further improve image quality, post-ADMIRE decluttered channel data can be combined with other beamforming techniques, including traditional linear apodization methods, minimum variance (MV) beamforming [16,18] or other advanced beamforming methods. Here, we consider an adaptive weighting approach based on the coherence factor (CF). The coherence factor (CF) is computed using delayed channel signals (i.e., aperture domain signals), defined as [12]

$$CF(k) = \frac{\left|\sum_{m=1}^{M} s(m,k)\right|^2}{M \sum_{m=1}^{M} |s(m,k)|^2},\tag{9}$$

where k is the discrete time index, m indexes aperture element, $s(m,k)$ is the delayed channel signal of element m, and M is the total number of receive aperture elements [10–12]. We apply CF weighting to

Table 1
ADMIRE parameters.

Parameter	Value
α	0.9
λ	$0.0189\sqrt{y^\top y}$
c_{lat}	4
c_{axl}	2
Model space (lateral)	aperture width
Model space (axial)	$z_r \pm (c_{axl}\,res_{axl})/2$
Model sampling (ROI)	$\{0.0716res_{lat}, 0.286res_{axl}\}$
Model sampling (clutter)	$\{1.43res_{lat}, 1.43res_{axl}\}$
STFT window size	$(8\log(2))/(2\pi BW f_c)$

⊤ is the matrix transpose.

BW is the fractional bandwidth.

f_c is the center frequency of transmitted pulse.

Table 2
Field II simulation parameters.

Parameter	Value
Number of aperture elements	128
Number of mathematical elements elevationally	11
Number of mathematical elements laterally	7
Height of element	8 mm
Width of element	0.254 mm
Kerf	0.003 mm
Lateral pitch	0.257 mm
Center frequency (f_c)	3 MHz
Sampling frequency (simulation)	120 MHz
Sampling frequency (downsampled)	40 MHz
Bandwidth	60%
Transmit focal depth	3 cm
Transmit/Receive f/#	2.0

Table 3
Curvilinear probe and system setting.

Parameter	Value
Sector	75°
Number of elements	128
Pitch	0.425 mm
Center frequency (f_c)	3.125 MHz
Sampling frequency (f_s)	12.5 MHz
Bandwidth	60%
Transmit focal depth	3 cm
Transmit/Receive f/#	1.0
Speed of sound (c)	1540 m/s
In water (c_w)	1480 m/s

beamformed radio-frequency (RF) signals obtained from DAS and ADMIRE, as a post-processing technique.

2.3. Simulations

We simulated a point target to demonstrate resolution performance and basic side-lobe suppression performance. We used Field II [38,39] to conduct the simulations using the parameters indicated in Table 2. We modeled a phase array transducer with 3.0 MHz center frequency and 60% fractional bandwidth. We compared point spread functions derived from DAS and ADMIRE beamforming. We also combined DAS and ADMIRE with CF weighting. The resulting point spread functions demonstrate spatial resolution and off-axis energy suppression of each beamforming approach. We then quantified the spatial resolution laterally and axially (i.e., the FWHM of the lateral and axial beam profiles).

We also simulated a resolution target phantom—meaning several adjacent point targets—using Field II to further evaluate the various algorithms. The simulated resolution phantom mimics a wire phantom image, which is composed of five point targets. We applied the same parameters, as indicated in Table 2. The resulting images of the resolution phantom were reconstructed using DAS and ADMIRE, along with CF weighting, denoted as DAS + CF and ADMIRE + CF.

Using the Field II, we continued to simulate a uniform, fully developed speckle background with a density of 25 scatterers per resolution cell [40], in the presence of a single strong scatterer. The Field II parameter settings were the same as indicated in Table 2. The single strong scatterer's amplitude was scaled, relative to the background scatterers. We generated imaging data ranging from a single scatterer-to-background speckle ratio (SBR) of 20 dB to 80 dB, given by

$$SBR = 10\log 10\left(\frac{P_{Scatterer}}{\overline{P}_{Bkg}}\right).\tag{10}$$

where $P_{Scatterer}$ and $\overline{P}_{Bkg}$ denote the power of the single scatterer and the
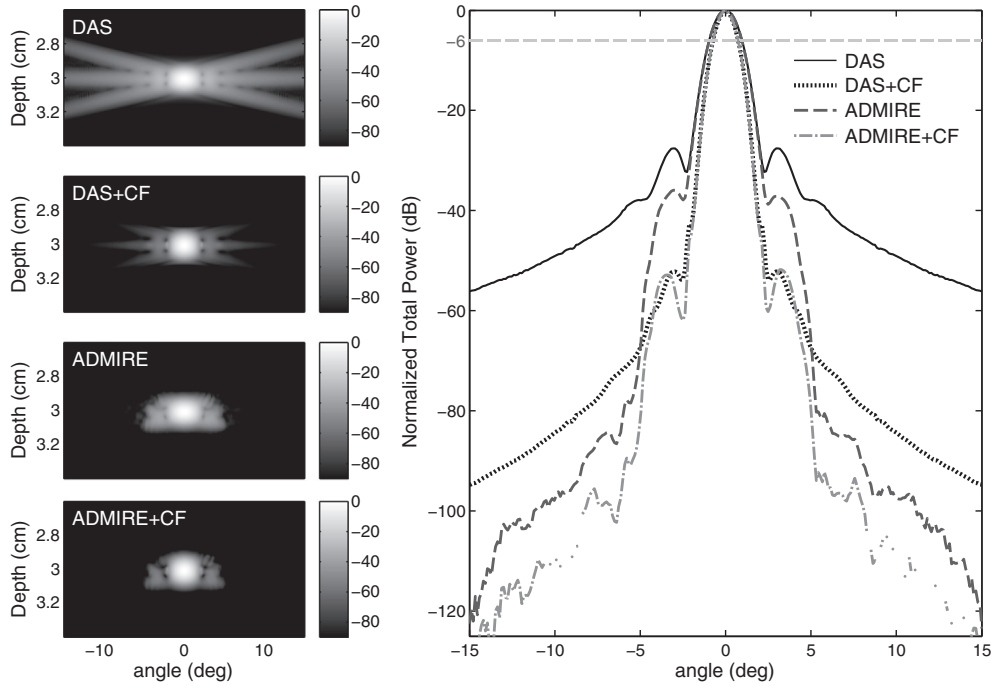
Fig. 2. Set of 2-D (left) and 1-D (right) point spread functions simulated using standard DAS, DAS + CF, ADMIRE and ADMIRE + CF. The 1-D lateral spread functions (right), which is axially integrated, demonstrate main lobe width and side-lobes level.

Table 4
Quantitative spatial resolution (−6 dB).

	DAS	DAS + CF	ADMIRE	ADMIRE + CF
Lateral (mm)	1.01	0.77	0.99	0.76
Axial (mm)	0.60	0.61	0.61	0.63

average power of background speckle signal, respectively. We then applied DAS, DAS + CF, ADMIRE and ADMIRE + CF, respectively. The resulting images from applying ADMIRE, ADMIRE + CF include two cases using different values of λ: one is $0.0189\sqrt{y^{\top}y}$, indicated in Table 1, while the other has $0.00189\sqrt{y^{\top}y}$. Lower values of λ increase degrees of freedom [34]. The degrees of freedom in the first case are in a range between 50 and 70 (i.e., low *df*), while those of the second case are nearly equal to the maximum allowable degrees of freedom (i.e., high *df*). We then evaluated ADMIRE performance.

Finally, we investigated the robustness of the methods in the presence of sound speed inhomogeneities using simulated data. We modeled a phased array transducer with 3.5 MHz center frequency and 60% fractional bandwidth, similar to the point spread function simulation setting summarized in Table 2. We used Field II to simulate the received pulse echo signals. The focal depth of the transmit beam was specified at 3 cm, with an f/1.5 system on both transmit and receive beams. The simulated phantoms were a resolution target and a contrast target. The resolution target phantom has a point target placed at 3 cm, while the contrast phantom is an anechoic cyst of a 5 mm diameter circle 3 cm deep in fully developed speckle background. The sound speeds used in the simulation were across a range of 10% above and below the assumed sound speed (i.e., 1540 m/s). We always applied beamforming delays assuming the sound speed was 1540 m/s.

We computed metrics of resolution and contrast as a function of sound speed mismatch. The spatial resolution was quantified by measuring lateral FWHM length in resolution target phantoms, while we computed contrast and contrast-to-noise ratio (CNR) using contrast target phantoms. The contrast and CNR metrics are defined by

$$C = -20\log10\left(\frac{\mu_L}{\mu_B}\right),$$
(11)

$$CNR = 20\log10\left(\frac{|\mu_L - \mu_B|}{\sqrt{\sigma_L^2 + \sigma_B^2}}\right),$$
(12)

where (μ_L, σ_L^2) and (μ_B, σ_B^2) denote the value of (mean, variance) of the enveloped but uncompressed image inside (i.e., lesion) and outside (i.e., background) the anechoic structures, respectively. Along with contrast and CNR, we also measured speckle statistics using

$$SNR_{\text{speckle}} = \frac{\mu_B}{\sigma_B}.$$
(13)

There are 6 independent speckle realizations generated for the contrast target simulation. We applied image quality metrics to data after DAS and ADMIRE with and without CF weighting.

2.4. Experimental phantom data

To reinforce the simulation results, we evaluated the methods using experimental data obtained from a wire phantom inside a water bath. We collected the experimental data using a Verasonics Vantage Ultrasound System (Verasonics, Inc., Kirkland, WA) and a C5-2 curvilinear array transducer. 128 A-lines were acquired over a 75° sector. Table 3 summarizes the operation settings for the curvilinear probe and the ultrasound system. The experimental data were processed using the same beamforming and post-processing methods as the simulated data.

Additionally, because we were interested in ADMIRE's ability to preserve speckle texture while suppressing off-axis clutter, we acquired imaging data from a tissue-mimicking phantom (Multi-Purpose Multi-Tissue Ultrasound Phantom 040GSE, CIRS Inc., Norfolk, Virginia, USA). We used the same settings as in the case of the wire phantom acquisition. The acquired data were reconstructed using the same beamformer with and without CF weighting before B-mode image formation. We quantified image quality metrics, including contrast ratio, CNR and speckle statistics of the B-mode image using the same equations of ()()() (11)–(13), respectively.
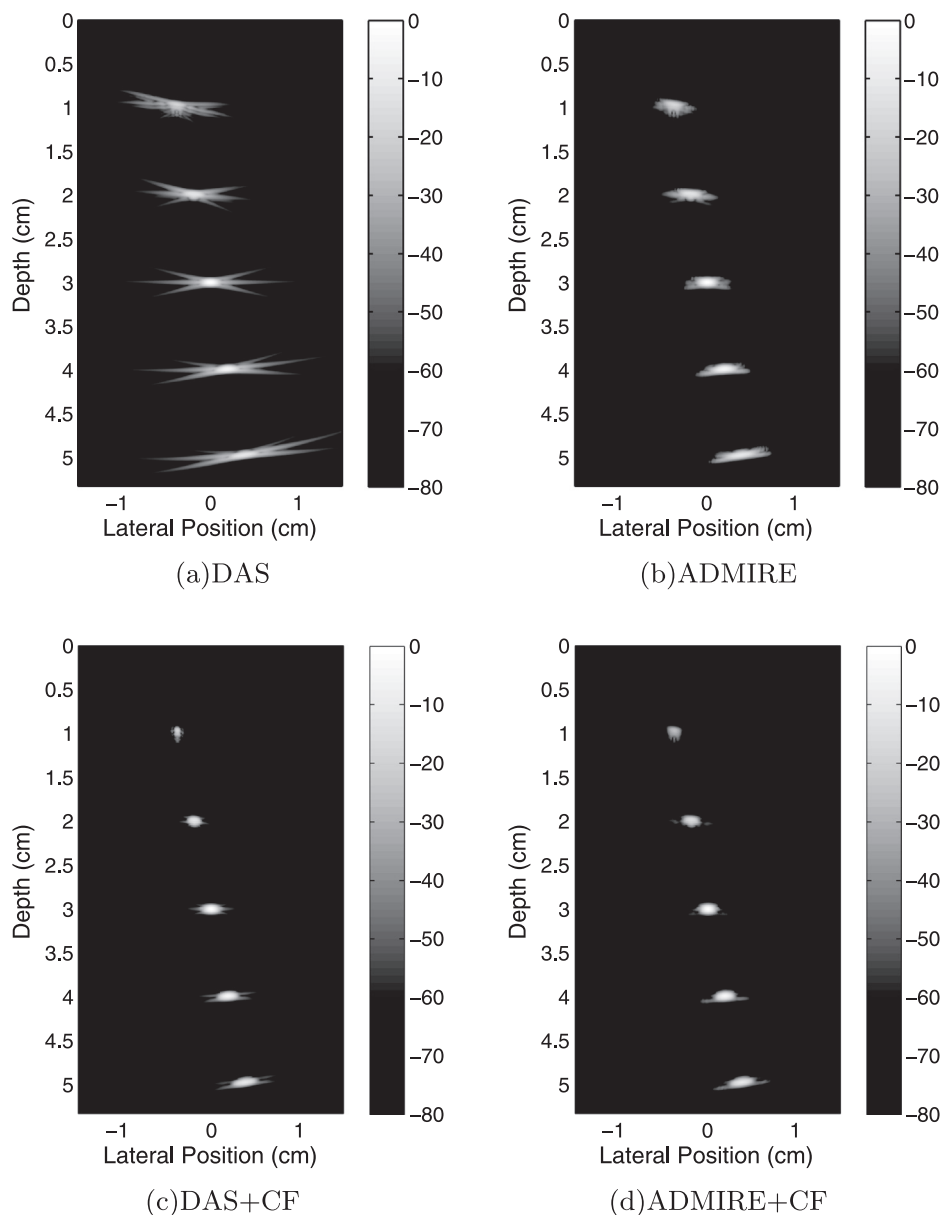
Fig. 3. Simulated resolution phantom images with five point targets, mimicking a wire phantom. The images are formed by using (a) standard DAS, (b) ADMIRE, (c) DAS + CF and (d) ADMIRE + CF. The resulting images can indicate off-axis energy suppression with focused and unfocused targets using each beamforming method. The dynamic range is 80 dB in order to highlight the side-lobes.

2.5. In vivo data

We acquired *in vivo* data from a human subject's liver using a Verasonics Vantage Ultrasound System (Verasonics, Inc., Kirkland, WA) and a C5-2 curvilinear array transducer. The acquisition parameters are the same as those in Table 3. After data acquisition, we formed B-mode images using DAS and ADMIRE with and without CF weighting. We evaluated the B-mode images qualitatively, while image quality metrics were used for quantitative measurements of the images obtained from each beamforming method. The study was approved by the Vanderbilt University Institutional Review Board.

3. Results

Fig. 2 shows the set of point spread functions in 2-D (left) and 1-D spaces (right). The spatial resolution is quantified laterally and axially, indicated in Table 4. The dynamic range of 2-D point spread function images is 90 dB. The 1-D lateral point spread function derived from

ADMIRE demonstrates that the first side-lobes are reduced to −40 dB and off-axis energy is suppressed below −100 dB, while the standard DAS reduced off-axis energy below −50 dB. Along with off-axis energy suppression, it is worth noting that the main-lobe width (−6 dB) of ADMIRE is practically unperturbed. These findings suggest that AD-MIRE substantially suppress off-axis energy arriving away from the received focus without any loss in lateral resolution, and that the CF can be integrated with ADMIRE as with DAS.

Fig. 2 also demonstrates that DAS + CF provides lower side-lobes and a narrower main lobe than DAS and ADMIRE. The combination of ADMIRE with CF weighting (ADMIRE + CF) may be the most beneficial with respect to improvement of image resolution and contrast based on the point target data.

Fig. 3 demonstrates the phantom images with five point targets using DAS, ADMIRE, DAS + CF and ADMIRE + CF. The images are shown with a dynamic range of 80 dB. When comparing these images, ADMIRE shows improvement over DAS, but DAS + CF provides better resolution image than ADMIRE, which is consistent with the 1-D point
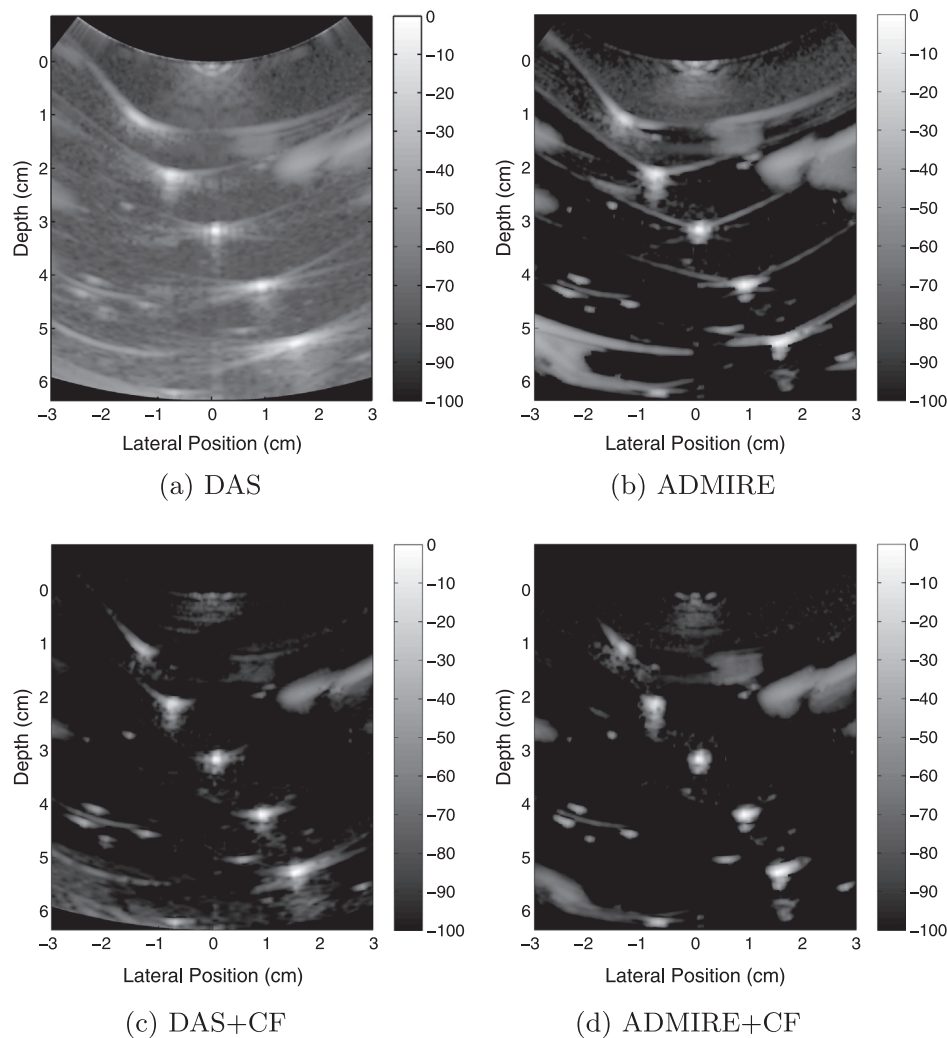
Fig. 4. The experimental wire phantom images reconstructed using four different beamforming methods: (a) DAS, (b) ADMIRE, (c) DAS + CF and (d) ADMIRE + CF. The results obtained from the experimental data are correlated with simulations. The dynamic range is 100 dB to highlight side-lobes and other clutter present. The data were beamformed using sound speed of 1480 m/s.

spread functions in Fig. 2. These resulting images also indicate that the combination of ADMIRE with CF weighting may be the best method, when considering only off-axis energy suppression and lateral image resolution.

Along with the simulation results, Figs. 4 and 5 present the experimental results obtained from the acquired data using a transducer and an ultrasound imaging system. Fig. 4 displays the wire phantom images reconstructed using DAS, ADMIRE, DAS + CF and AD-MIRE + CF. The resulting images are based on a dynamic range of 100 dB. Comparing four wire images, it is apparent that the use of CF weighting to DAS beamforming significantly improves the wire phantom image, while ADMIRE + CF also shows some improvement compared to the ADMIRE image, suggesting that ADMIRE + CF still provides the best image quality of these four images. The findings from the wire phantom images are consistent with the simulation results we demonstrated. Table 5 summarizes lateral and axial resolutions measured from the images in Figs. 3 and 4. However, when evaluating quantitative results in Table 5, both lateral and axial resolutions at 3 cm focus are slightly better with ADMIRE than DAS + CF in the case of wire phantom, which is inconsistent with simulation results. In general, the −6 dB resolution is not changed in a meaningful way, which is consistent with the way ADMIRE was implemented here.

We also evaluated ADMIRE performance with background speckle texture using a tissue-mimicking phantom. Four tissue-mimicking

phantom B-mode images are demonstrated in Fig. 5. When carefully looking into these images, the ADMIRE may provide high contrast in and around existing cysts. Although adding CF does improve contrast and resolution as expected, it also reduces the background speckle SNR. Table 6 summarizes the quantitative results of image quality metrics and speckle statistics in each B-mode image. When comparing the values of measured contrast and CNR, ADMIRE outperforms DAS itself. It is important to note that ADMIRE largely preserves speckle statistics, especially, when compared with the CF weighting method.

Our evaluation of ADMIRE also identified some limitations that are consistent with other advanced beamformers [41]. Fig. 6 exemplifies the limitation using a fully developed speckle background with a single bright scatterer. When the single scatterer is 20 dB or even 40 dB higher compared to the background speckle signal, neither DAS nor ADMIRE B-mode images show any noticeable difference, but images with CF weighting decrease speckle texture, especially around the strong scatterer. However, as the ratio between a strong scatterer to the background signal increases, the image resulting from the application of ADMIRE with low degrees of freedom suppresses the background signal in the region of the side-lobes, similar to the CF images. However, DAS maintains background speckle, but the off-axis clutter from the bright scatterer persists. The trend is more definitive when a single scatterer is very strong such as the ratio 60 dB or 80 dB. When comparing the two ADMIRE B-mode images using low and high degrees of freedom, it is
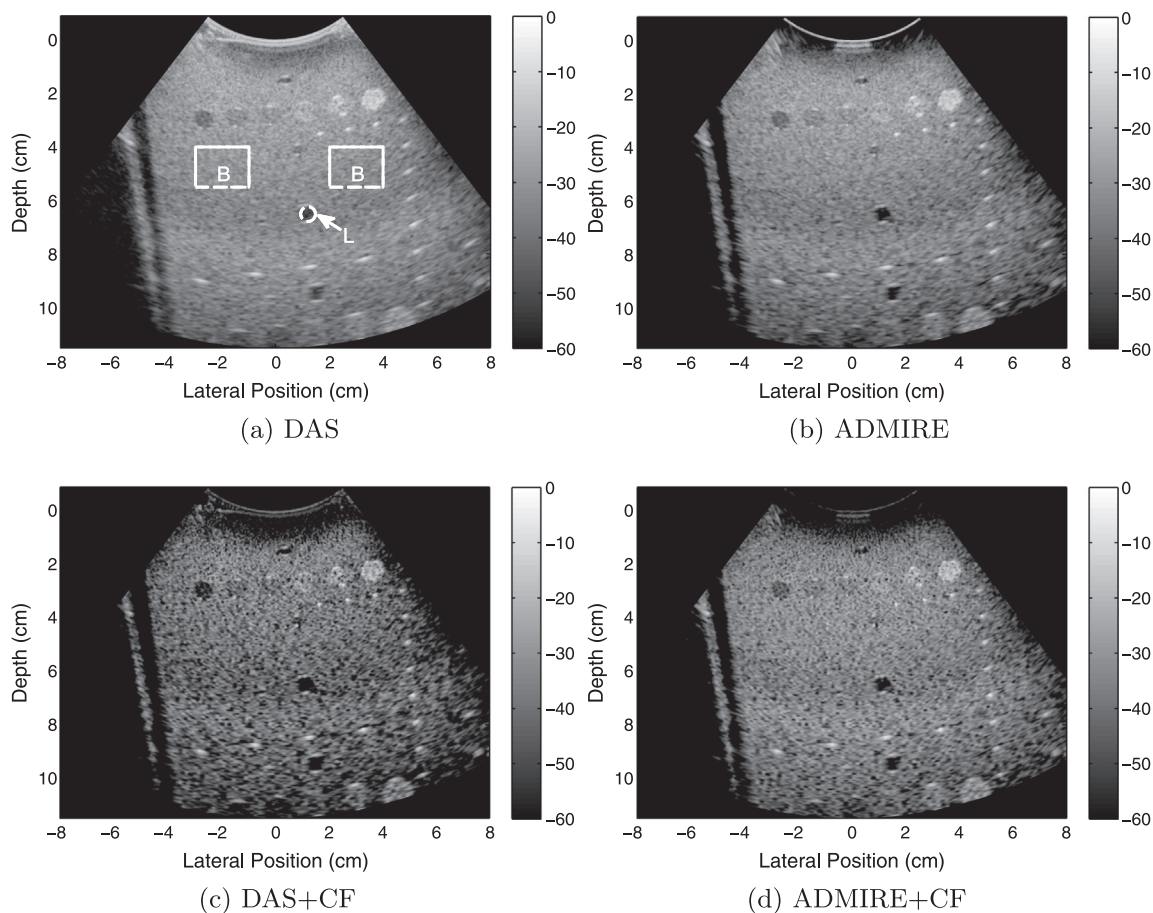
Fig. 5. Tissue mimicking phantom images formed using (a) DAS, (b) ADMIRE, (c) DAS + CF and (d) ADMIRE + CF. The dynamic range is 60 dB. The DAS image in (a) also shows two enclosed areas by white dashed lines and a circle by white solid line (i.e., mask regions) that were used to quantify contrast, contrast-to-noise ratio (CNR) and speckle signal-to-noise ratio (SNR$_{speckle}$) for each imaging data. An 'L' or 'B' denotes lesion or background, respectively.

Table 5
Quantitative Spatial Resolutions (-6 dB) of Figs. 3 and 4

Simulated resolution phantom		DAS	DAS + CF	ADMIRE	ADMIRE + CF
Lateral (mm)	@(-0.4, 1.0) cm	1.49	1.09	1.42	1.03
	@(-0.2, 2.0) cm	1.75	1.26	1.73	1.23
	@(0, 3.0) cm	1.09	0.90	1.04	0.83
	@(0.2, 4.0) cm	1.56	1.23	1.50	1.15
	@(0.4, 5.0) cm	2.41	1.73	2.35	1.67
	$\mu_{lateral} \pm \sigma_{lateral}$	1.66 ± 0.48	1.24 ± 0.31	1.61 ± 0.49	1.18 ± 0.31
axial (mm)	@(-0.4, 1.0) cm	0.57	0.62	0.60	0.64
	@(-0.2, 2.0) cm	0.56	0.57	0.58	0.59
	@(0, 3.0) cm	0.43	0.45	0.46	0.48
	@(0.2, 4.0) cm	0.42	0.44	0.46	0.48
	@(0.4, 5.0) cm	0.42	0.43	0.43	0.45
	$\mu_{axial} \pm \sigma_{axial}$	0.48 ± 0.08	0.50 ± 0.09	0.51 ± 0.08	0.53 ± 0.08
Experimental wire phantom		DAS	DAS + CF	ADMIRE	ADMIRE + CF
Lateral (mm)	@(-1.5, 1.0) cm	1.40	1.24	1.29	1.23
	@(-1.0, 2.0) cm	1.71	1.36	1.40	1.40
	@(0, 3.0) cm	1.43	1.41	1.40	1.36
	@(1.0, 4.0) cm	1.59	1.19	1.44	1.35
	@(1.5, 5.0) cm	1.99	1.61	1.72	1.66
	$\mu_{lateral} \pm \sigma_{lateral}$	1.63 ± 0.24	1.37 ± 0.17	1.45 ± 0.16	1.40 ± 0.16
Axial (mm)	@(-1.5, 1.0) cm	1.13	1.11	1.05	1.08
	@(-1.0, 2.0) cm	1.15	1.07	0.89	1.01
	@(0, 3.0) cm	0.78	0.79	0.77	0.78
	@(1.0, 4.0) cm	0.84	0.83	0.85	0.83
	@(1.5, 5.0) cm	0.86	0.85	0.75	0.74
	$\mu_{axial} \pm \sigma_{axial}$	0.95 ± 0.18	0.93 ± 0.15	0.86 ± 0.12	0.88 ± 0.15

Table 6
Image quality metrics and speckle statistics.

Beamforming	Contrast (dB)	CNR (dB)	SNR$_{speckle}$
DAS	13.80	2.65	1.78
ADMIRE	17.33	2.71	1.68
DAS + CF	17.34	−1.29	1.03
ADMIRE + CF	18.40	0.72	1.39

apparent that image artifacts around a bright scatterer (i.e., dark region) decrease when implementing ADMIRE with high degrees of freedom; especially, in the case of 60 dB. These results suggest that ADMIRE performance and its limitations depend on deliberate selection of the regularization parameters, especially λ, which sets the degrees of freedom.

Figs. 7 and 8 demonstrate the impact of sound speed errors on ADMIRE performance. In Fig. 7, ADMIRE shows lower lateral FWHM (i.e., better lateral resolution) than DAS, particularly, in the range of sound speed below 1540 m/s. (Note that Fig. 7 (d) reports that the lowest FWHM is measured at $c_{actual}/c_{assumed} = 0.98$ when applying AD-MIRE and ADMIRE + CF.) It is noted that DAS + CF and ADMIRE + CF show better resolution than DAS and ADMIRE over the range of sound speed variation. It is also worth noting that the impact of sound speed errors largely mimics traditional beamforming (i.e., standard DAS) and ADMIRE never does worse.

The impact of sound speed inhomogeneities is shown in Fig. 8, which shows contrast, CNR and speckle SNR. In general, ADMIRE does not do worse than DAS for moderate deviations in sound speed despite being model-based, which is based on an assumed sound speed. It is interesting that the peak contrast for ADMIRE does occur at a slightly lower sound speed than for DAS, which is consistent with the results seen in Fig. 7.

Fig. 9 shows four *in vivo* images formed by applying DAS and AD-MIRE, before and after CF weighting. We also measured contrast, CNR and SNR$_{speckle}$, as indicated in Table 7. The quality of the resulting *in vivo* B-mode images suggest that ADMIRE suppresses clutter and provides well-delineated anatomy (i.e., lesions) while preserving tissue speckle texture. However, use of CF weighting after applying DAS and ADMIRE may degrade speckle texture, resulting in lower CNR and lower SNR$_{speckle}$. The values of image quality metrics and speckle

statistics in Table 7 are consistent with the qualitative evaluation of Fig. 9. These findings from *in vivo* data are also correlated with results from simulations and experimental phantoms.

4. Discussion

We investigated the robustness of model-based beamforming in the presence of off-axis clutter and sound speed inhomogeneities. The results from simulations and experimental phantom data in Figs. 2–4 demonstrate that ADMIRE is useful to substantially reduce off-axis artifacts in B-mode images, and offers flexible features to combine with other beamforming methods. In this study, we show that ADMIRE with CF weighting further improves some aspects of image quality. There are, however, some drawbacks of using CF as an adaptive weighting method. The resulting images after the CF weighting show slightly decreased axial resolution as indicated in Tables 4 and 5, and the CF weighted images also have lower CNR and lower SNR compared to the images without CF weighing. This is primarily driven by the degradation of background speckle, which is a known problem with CF like techniques. Some of these effects can be mitigated by using the generalized coherence factor (GCF) introduced by Li et al. [12]. However, we did not use it to avoid introducing an additional confusing parameter in this study.

We also identified ADMIRE's potential limitations in suppressing clutter, as shown in Fig. 6. ADMIRE still has a higher dynamic range than DAS [42]. The results suggest that in some cases ADMIRE may discard wanted signals (i.e., signals of interest), particularly, when low degrees of freedom are used in the presence of high levels of clutter. In general, it is necessary to use higher degrees of freedom with higher clutter scenarios when implementing ADMIRE. For example, applying ADMIRE, with higher degrees of freedom (i.e., lower λ value), mitigated dark region artifacts around a bright scatterer in an image, as demonstrated in Fig. 6. It can thus be suggested that it is possible to address these limitations by carefully selecting the ADMIRE tuning parameters. The deliberate selection of ADMIRE parameters may also increase ADMIRE's dynamic range [42]. Dynamic range is an underappreciated quality factor of ultrasound beamforming.

In simulations, we demonstrated that ADMIRE is also robust in the presence of sound speed mismatch. Fig. 7 demonstrates that ADMIRE outperforms DAS in lateral resolution within the range of sound speed
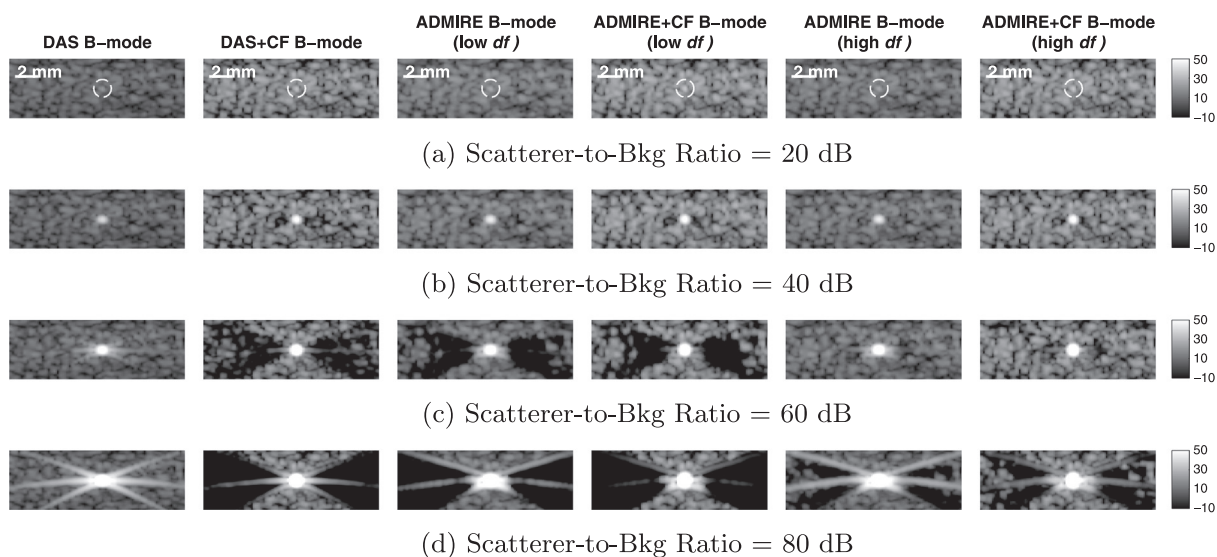
Fig. 6. Speckle-based target simulations in the presence of a strong scatterer (circled) underlying background speckle to identify potential limitations of the various beamforming methods. The strong scatterer is scaled by a scatterer-to-background ratio (SBR) 20 dB, 40 dB, 60 dB and 80 dB. We then apply DAS, DAS + CF, ADMIRE and ADMIRE + CF to compare the resulting images. Two sets of the resulting images from applying ADMIRE and ADMIRE + CF are with low and high degrees of freedom (*df*) cases. The images are scaled so that the speckle background is at 0 dB. The dynamic range of all images is 60 dB (i.e., −10 to 50 dB).

(a) $c_{actual}/c_{assumed} = 0.9$

(b) $c_{actual}/c_{assumed} = 1.0$

(c) $c_{actual}/c_{assumed} = 1.1$

(d) FWHM length as a function of sound speed variation
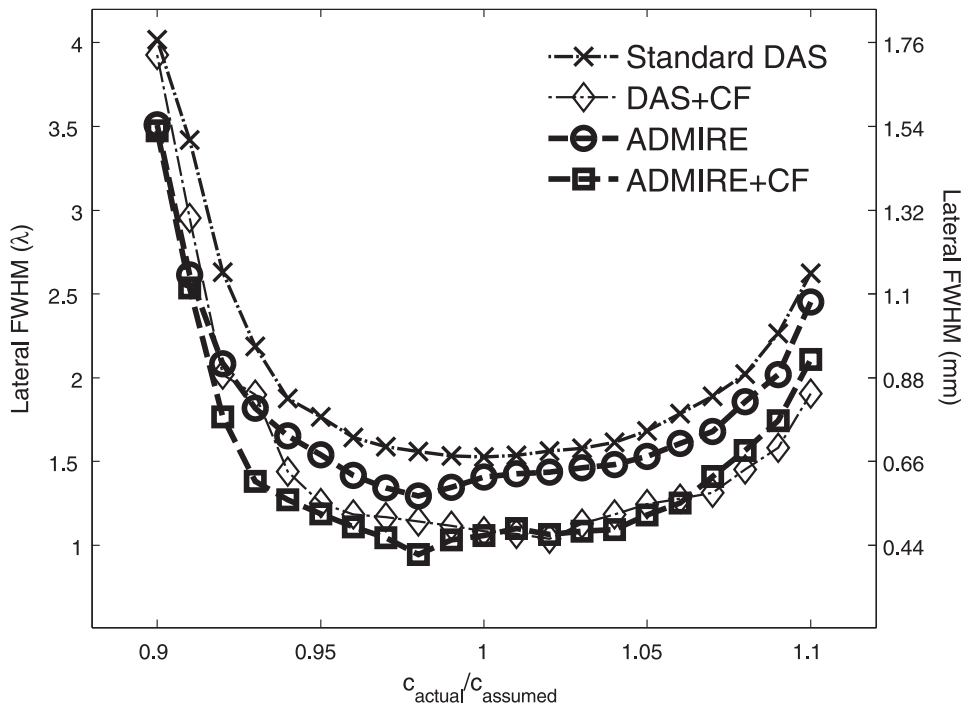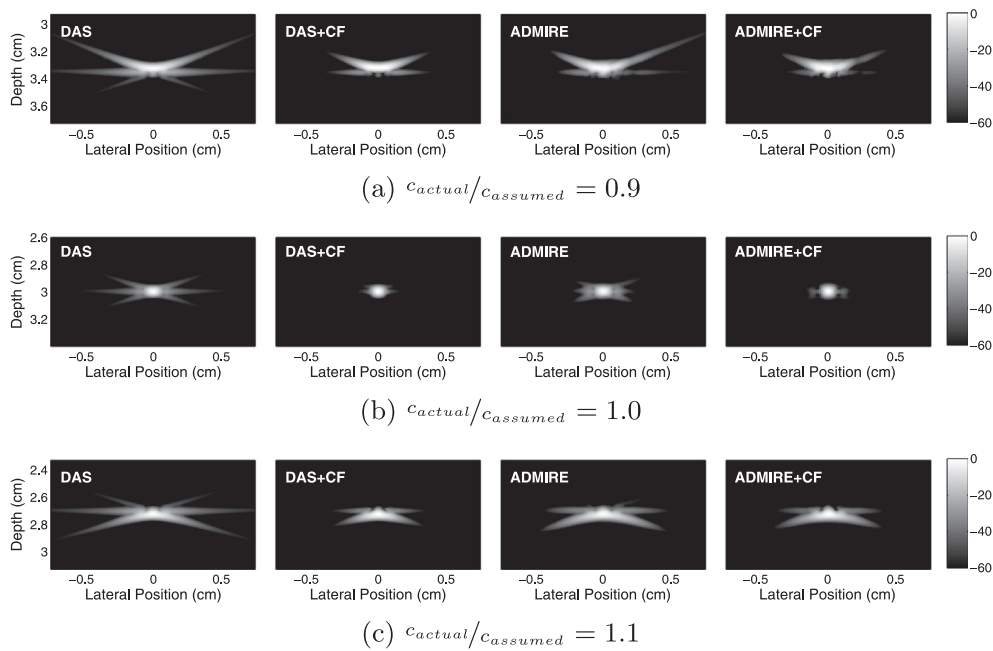
Fig. 7. The full-width and half-maximum (FWHM) beam width at the peak on-axis as a function of sound speed error. We apply the assumed sound speed, $c_{assumed} = 1540$ m/s, and the range of deviation is ±10%. The resolution target phantom images obtained from four beamforming methods, with (a) −10%, (b) 0% and (c) + 10% sound speed variation, are shown. The lateral FWHM lengths as a function of sound speed variation are plotted in (d).

variation. We show that the benefits of CF on DAS largely hold for ADMIRE, as well. In evaluating ADMIRE performance using anechoic cyst phantoms, we quantified contrast and CNR using the data inside and outside an anechoic cyst, along with speckle statistics of outside (i.e., background). Referring to Fig. 8, although ADMIRE is largely robust to sound speed, it is clear that CNR and SNR$_{speckle}$ does degrade with large sound speed mismatch. It is also worth noting that DAS + CF and ADMIRE + CF beamforming boosts contrast, compared to DAS and ADMIRE alone, but the CNR and SNR$_{speckle}$ are shown to be much lower than those of DAS and ADMIRE. These findings are consistent with the

results reported from tissue-mimic phantom experiment and *in vivo* liver data.

One unexpected finding in this simulation is that the cases applying ADMIRE, with and without CF weighting, provide the best resolution and the highest image contrast at lower sound speed than the beam-formed sound speed; e.g., the post-ADMIRE lateral FWHM has the shortest length at $c_{actual}/c_{assumed} = 0.98$, while contrast measured after ADMIRE show the highest peak occurred at $c_{actual}/c_{assumed} = 0.97$. A possible explanation for these results may be related to degrees of freedom selected when implementing ADMIRE. Because gross sound

(a) $c_{actual}/c_{assumed} = 0.9$

(b) $c_{actual}/c_{assumed} = 1.0$

(c) $c_{actual}/c_{assumed} = 1.1$
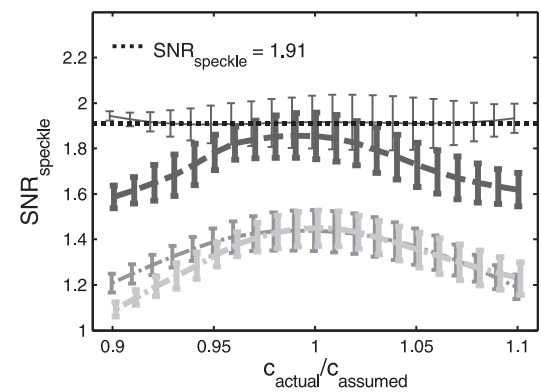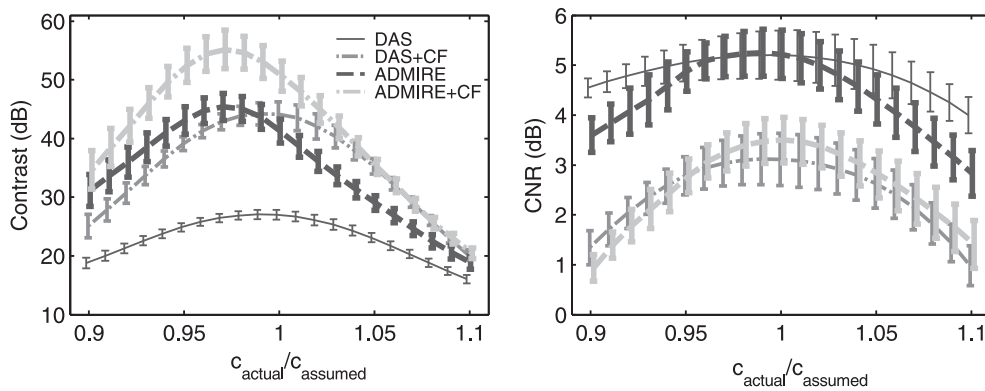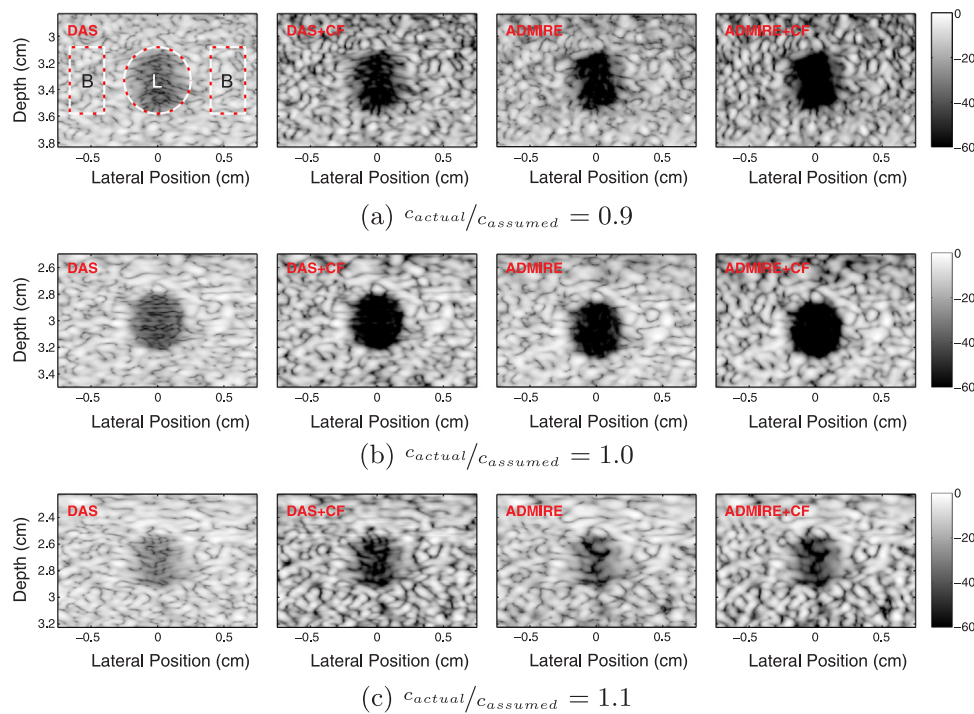
(d) Contrast, CNR and SNR$_{speckle}$ as a function of sound speed variation

Fig. 8. The measurements of contrast, CNR and speckle SNR (SNR$_{speckle}$) as a function of sound speed mismatch. The assumed sound speed is $c_{assumed} = 1540$ m/s with the range of deviation of ±10%. The anechoic cyst images formed from four beamforming methods are presented in sound speed mismatch of (a) −10%, (b) 0% and (c) + 10%. The DAS in (a) also shows mask regions that were used to quantify contrast, CNR and SNR$_{speckle}$ for each image. The regions are indicated by the red and white contour lines with an 'L' or 'B', denoting lesion or background, respectively. The measurement results of contrast, CNR and SNR$_{speckle}$ are demonstrated in (d).

speed deviation increases acoustic clutter, the required degrees of freedom of optimal imaging may increase. As an artifact of this, the resolution appears to improve but eventually at the lost of speckle

texture.

Finally, we applied ADMIRE to *in vivo* liver data to assess the results obtained from simulations and phantom experiments. It is no surprise

(a) DAS

(b) ADMIRE
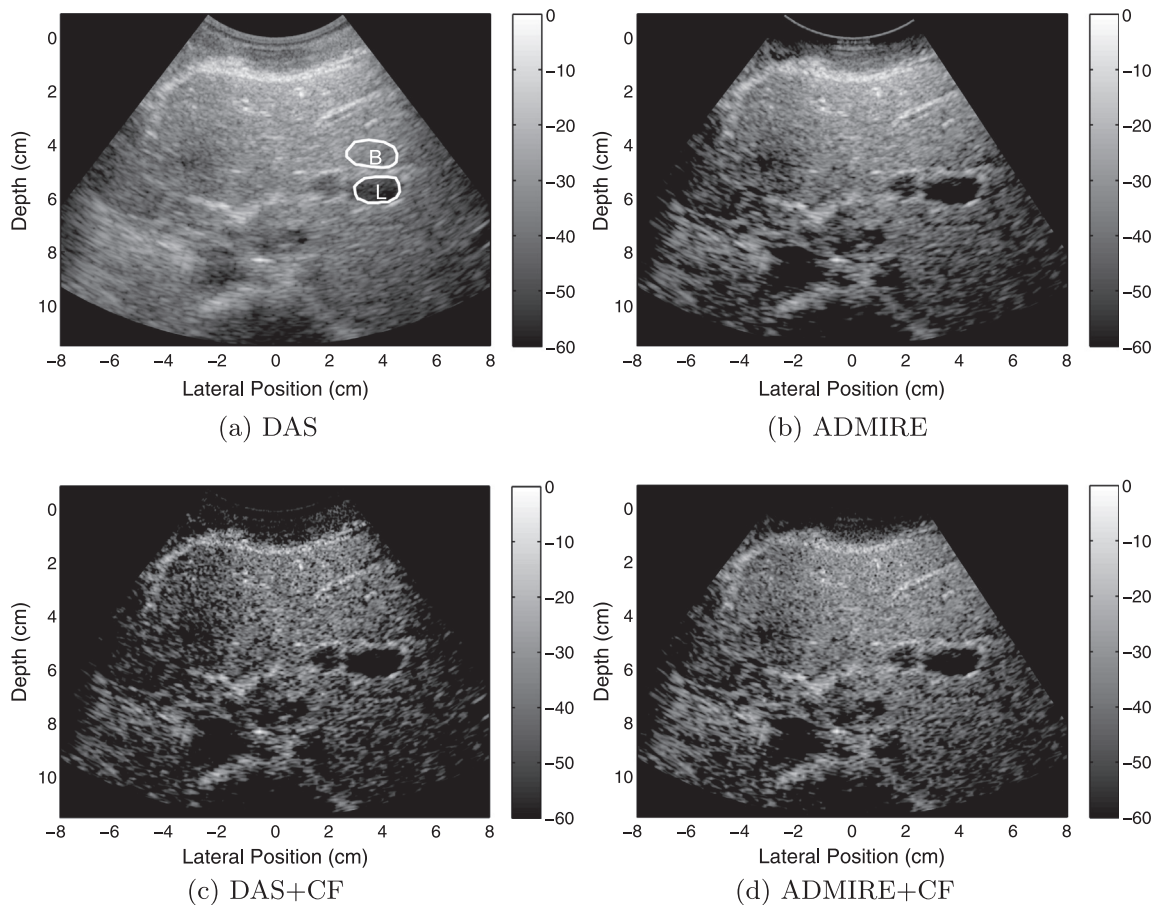
(c) DAS+CF

(d) ADMIRE+CF

Fig. 9. *In vivo* liver images reconstructed using (a) DAS, (b) ADMIRE, (c) DAS + CF and (d) ADMIRE + CF. The dynamic range is 60 dB. The DAS image in (a) also includes mask regions indicated by the white contour lines with an 'L' or 'B', denoting lesion or background, respectively. The regions were used to measure contrast, contrast-to-noise ratio (CNR) and speckle signal-to-noise ratio (SNR$_{speckle}$) for each B-mode image.

Table 7
In vivo image quality metrics and speckle statistics.

Beamforming	Contrast (dB)	CNR (dB)	SNR$_{speckle}$
DAS	17.22	3.75	1.82
ADMIRE	28.61	3.63	1.61
DAS + CF	28.25	0.70	1.13
ADMIRE + CF	29.58	1.66	1.27

that the ADMIRE B-mode image has a boost over 10 dB in contrast compared with the DAS B-mode image, as indicated in Table 7. It could be possible that the ADMIRE *in vivo* images could improve further implementing ADMIRE with a complete model space that also accounts for reverberation clutter. But, the results from the *in vivo* data are largely consistent with the findings from simulations and phantom experiments.

5. Conclusions

In this study, we demonstrated that ADMIRE, a model-based beamforming algorithm, substantially suppresses off-axis clutter while preserving resolution, compared to images obtained from DAS. By using post-ADMIRE decluttered channel data, we also showed that ADMIRE, combined with other algorithms, further improves some image metrics. Finally, we demonstrated that ADMIRE is robust to model-mismatch caused by gross sound speed mismatch, indicating its usefulness in real-clinical applications.

Appendix A. Supplementary mateiral

Supplementary data associated with this article can be found, in the online version, at http://dx.doi.org/10.1016/j.ultras.2018.04.011.

References

[1] T.L. Szabo, Diagnostic Ultrasound Imaging: Inside Out, Academic Press, 2004.
[2] J.E. Aldrich, Basic physics of ultrasound imaging, Critical Care Med. 35 (5) (2007) S131–S137.
[3] R.S. Cobbold, Foundations of Biomedical Ultrasound, Oxford University Press on Demand, 2007.
[4] M.E. Anderson, G.E. Trahey, The direct estimation of sound speed using pulse–echo ultrasound, J. Acoust. Soc. Am. 104 (5) (1998) 3099–3106.
[5] M. Anderson, M. McKeag, G. Trahey, The impact of sound speed errors on medical ultrasound imaging, J. Acoust. Soc. Am. 107 (6) (2000) 3540–3548.
[6] S. Flax, M. O'Donnell, Phase-aberration correction using signals from point reflectors and diffuse scatterers: basic principles, IEEE Trans. Ultrason., Ferroelectr., Freq. Control 35 (6) (1988) 758–767.
[7] G. Pinton, G.E. Trahey, Dahl, Erratum: sources of image degradation in fundamental and harmonic ultrasound imaging using nonlinear, full-wave simulations, IEEE Trans. Ultrason., Ferroelectr., Freq. Control 58 (6) (2011) 1272–1283.
[8] B. Byram, M. Jakovljevic, Ultrasonic multipath and beamforming clutter reduction: a chirp model approach, IEEE Trans. Ultrason., Ferroelectr., Freq. Control 61 (3) (2014) 428–440.
[9] J.T. Bushberg, J.M. Boone, The Essential Physics of Medical Imaging, Lippincott Williams & Wilkins, 2011.
[10] R. Mallart, M. Fink, Adaptive focusing in scattering media through sound-speed

inhomogeneities: the van Cittert Zernike approach and focusing criterion, J. Acoust. Soc. Am. 96 (6) (1994) 3721–3732.

[11] K. Hollman, K. Rigby, M. O'donnell, Coherence factor of speckle from a multi-row probe, Proceedings of the 1999 IEEE Ultrasonics Symposium, vol. 2, IEEE, 1999, pp. 1257–1260.

[12] P.-C. Li, M.-L. Li, Adaptive imaging using the generalized coherence factor, IEEE Trans. Ultrason., Ferroelectr., Freq. Control 50 (2) (2003) 128–141.

[13] J. Camacho, M. Parrilla, C. Fritsch, Phase coherence imaging, IEEE Trans. Ultrason., Ferroelectr., Freq. Control 56 (5) (2009).

[14] J. Synnevag, A. Austeng, S. Holm, Minimum variance adaptive beamforming applied to medical ultrasound imaging, in: Proceedings of the IEEE Ultrasonics Symposium, vol. 2, 2005, pp. 1199–1202.

[15] Z. Wang, J. Li, R. Wu, Time-delay-and time-reversal-based robust capon beamformers for ultrasound imaging, IEEE Trans. Med. Imag. 24 (10) (2005) 1308–1322.

[16] J. Synnevag, A. Austeng, S. Holm, Adaptive beamforming applied to medical ultrasound imaging, IEEE Trans. Ultrason. Ferroelectr. Freq. Control 54 (8) (2007) 1606.

[17] B.M. Asl, A. Mahloojifar, Minimum variance beamforming combined with adaptive coherence weighting applied to medical ultrasound imaging, IEEE Trans. Ultrason., Ferroelectr., Freq. Control 56 (9) (2009) 1923–1931.

[18] I.K. Holfort, F. Gran, J.A. Jensen, Broadband minimum variance beamforming for ultrasound imaging, IEEE Trans. Ultrason., Ferroelectr., Freq. Control 56 (2) (2009) 314–325.

[19] C.H. Seo, J. Yen, Sidelobe suppression in ultrasound imaging using dual apodization with cross-correlation, IEEE Trans. Ultrason., Ferroelectr., Freq. Control 55 (10) (2008) 2198–2210.

[20] C.H. Seo, J.T. Yen, Evaluating the robustness of dual apodization with cross-correlation, IEEE Trans. Ultrason., Ferroelectr., Freq. Control 56 (2) (2009) 291–303.

[21] J. Shin, J.T. Yen, Synergistic enhancements of ultrasound image contrast with a combination of phase aberration correction and dual apodization with cross-correlation, IEEE Trans. Ultrason., Ferroelectr., Freq. Control 59 (9) (2009).

[22] J.H. Sung, J.S. Jeong, Dual-/tri-apodization techniques for high frequency ultrasound imaging: a simulation study, Biomed. Eng. Online 13 (1) (2014) 1.

[23] D.A. Guenther, W.F. Walker, Optimal apodization design for medical ultrasound using constrained least squares part I: theory, IEEE Trans. Ultrason., Ferroelectr., Freq. Control 54 (2) (2007) 332–342.

[24] D.A. Guenther, W.F. Walker, Optimal apodization design for medical ultrasound using constrained least squares part II simulation results, IEEE Trans. Ultrason., Ferroelectr., Freq. Control 54 (2) (2007) 343–358.

[25] Z. He, F. Zheng, Y. Ma, H.H. Kim, Q. Zhou, K.K. Shung, A sidelobe suppressing near-field beamforming approach for ultrasound array imaging, J. Acoust. Soc. Am. 137 (5) (2015) 2785–2790.

[26] M.K. Jeong, S.J. Kwon, Estimation of side lobes in ultrasound imaging systems, Biomed. Eng. Lett. 5 (3) (2015) 229–239.

[27] B. Byram, Ultrasonic reverberation and off-axis clutter suppression using aperture domain signal decomposition, in: SPIE Medical Imaging, International Society for Optics and Photonics, 2013, 86750T–86750T.

[28] B. Byram, K. Dei, D. Dumont, An improved acoustic clutter model and direct in vivo assessment of off-axis and multipath clutter energy in the liver, 2014 IEEE International Ultrasonics Symposium (IUS), IEEE, 2014, pp. 531–534.

[29] B. Byram, K. Dei, J. Tierney, D. Dumont, A model and regularization scheme for ultrasonic beamforming clutter reduction, IEEE Trans. Ultrason., Ferroelectr., Freq. Control 62 (11) (2015) 1913–1927.

[30] K. Dei, B. Byram, The impact of model-based clutter suppression on cluttered, aberrated wavefronts, IEEE Trans. Ultrason., Ferroelectr., Freq. Control 64 (10) (2017) 1450–1464.

[31] B. Byram, J. Shu, K. Dei, Nonlinear beamforming of aperture domain signals, 2015 IEEE International Ultrasonics Symposium (IUS), IEEe, 2015, pp. 1–6.

[32] A. Selfridge, G. Kino, B. Khuri-Yakub, A theory for the radiation pattern of a narrow-strip acoustic transducer, Appl. Phys. Lett. 37 (1) (1980) 35–36.

[33] H. Zou, T. Hastie, Regularization and variable selection via the elastic net, J. R. Statist. Soc.: Ser. B (Statist. Methodol.) 67 (2) (2005) 301–320.

[34] R.J. Tibshirani, J. Taylor, et al., Degrees of freedom in lasso problems, Ann. Statist. 40 (2) (2012) 1198–1232.

[35] K. Dei, J. Tierney, B. Byram, Aperture domain model image reconstruction (ADMIRE) with plane wave synthesis, in: SPIE Medical Imaging 2017: Ultrasonic Imaging and Tomography, vol. 10139, International Society for Optics and Photonics, 2017, 1013911-1013911–10.

[36] X. Lv, G. Bi, C. Wan, M. Xing, Lv's distribution: principle, implementation, properties, and performance, IEEE Trans. Sig. Process. 59 (8) (2011) 3576–3591.

[37] B. Yang, A study of inverse short-time Fourier transform, in: 2008 IEEE International Conference on Acoustics, Speech and Signal Processing, 2008, pp. 3541–3544.

[38] J.A. Jensen, N.B. Svendsen, Calculation of pressure fields from arbitrarily shaped, apodized, and excited ultrasound transducers, IEEE Trans. Ultrason., Ferroelectr., Freq. Control 39 (2) (1992) 262–267.

[39] J.A. Jensen, Field: a program for simulating ultrasound systems, in: 10TH Nordicbaltic Conference on Biomedical Imaging, vol. 4(supplement 1, Part 1), Citeseer, 1996, pp. 351–353.

[40] R.F. Wagner, S.W. Smith, J.M. Sandrik, H. Lopez, Statistics of speckle in ultrasound B-scans, IEEE Trans. Sonics Ultrason. 30 (3) (1983) 156–163.

[41] O.M.H. Rindal, A. Rodriguez-Molares, A. Austeng, The dark region artifact in adaptive ultrasound beamforming, 2017 IEEE International Ultrasonics Symposium (IUS), IEEE, 2017, pp. 1–4.

[42] K. Dei, A. Luchies, B. Byram, Contrast ratio dynamic range: a new beamformer performance metric, 2017 IEEE International Ultrasonics Symposium (IUS), IEEE, 2017, pp. 1–4.